

## Perpendicular magnetic anisotropy in conducting NiCo<sub>2</sub>O<sub>4</sub> films from spin-lattice coupling

Corbyn Mellinger <sup>1</sup>, Jace Waybright <sup>1,2</sup>, Xiaozhe Zhang <sup>1,3</sup>, Caleb Schmidt <sup>1</sup>, and Xiaoshan Xu <sup>1,4</sup>

<sup>1</sup>*Department of Physics and Astronomy, University of Nebraska, Lincoln, Nebraska 68588, USA*

<sup>2</sup>*Department of Physics, South Dakota State University, Brookings, South Dakota 57007 USA*

<sup>3</sup>*School of Materials Science and Engineering, Xi'an Polytechnic University, Xi'an 710049, Xi'an, China*

<sup>4</sup>*Nebraska Center for Materials and Nanoscience, University of Nebraska, Lincoln, Nebraska 68588, USA*



(Received 5 November 2019; published 10 January 2020)

High perpendicular magnetic anisotropy (PMA), a property needed for nanoscale spintronic applications, is rare in oxide conductors. We report the observation of a PMA up to 0.23 MJ/m<sup>3</sup> in modestly strained (−0.3%) epitaxial NiCo<sub>2</sub>O<sub>4</sub> films which are room-temperature ferrimagnetic conductors. Spin-lattice coupling manifested as magnetoelastic effect was found as the origin of the PMA. The in-plane  $x^2$ - $y^2$  states of Co on tetrahedral sites play crucial role in the magnetic anisotropy and spin-lattice coupling with an energy scale of 1 meV/f.u. The elucidation of the microscopic origin paves a way for engineering oxide conductors for PMA using metal/oxygen hybridizations.

DOI: [10.1103/PhysRevB.101.014413](https://doi.org/10.1103/PhysRevB.101.014413)

Materials and heterostructures of high magnetic anisotropy have been increasingly demanded for energy and information applications. In particular, electrodes with perpendicular magnetic anisotropy (PMA) is needed in nanoscale spintronic devices for their high thermal stability and energy-efficient switching. Most materials or heterostructures of high PMA are based on intermetallic compounds [1–5], multilayers [6,7], or metal/oxide interfaces [8], often with high-cost elements such as Au and Pt. In contrast, transition-metal oxide conductors, despite their advantage of low-cost and structural and chemical stabilities, have rarely been reported to exhibit high PMA.

High magnetic anisotropy originates from structural anisotropy and spin-orbit coupling. In ordered intermetallic compounds containing strongly spin-orbit coupled nonmagnetic (NM) metals (e.g., Pd, Au, and Pt) and ferromagnetic (FM) metals (e.g., Fe and Co), anisotropic crystal structures lead to anisotropic hybridization between the states in NM and FM and consequently high magnetic anisotropy ( $\approx 5$  MJ/m<sup>3</sup>) [1–5,9]. The structural anisotropy can also be introduced by stacking NM and FM layers for high PMA ( $\approx 1$  MJ/m<sup>3</sup>) [7]. On the other hand, remarkable PMA has been demonstrated in Co/Ni multilayers ( $\approx 0.5$  MJ/m<sup>3</sup>) [6] and FM/oxide interfaces ( $\approx 0.2$  MJ/m<sup>3</sup>) [8,10,11], without the need for the strongly spin-orbit coupled NM. Here, the electronic degeneracy and occupancy are adjusted such that, the 3*d* states in FM with a large orbital angular momentum (in-plane states) determine the magnetic anisotropy. In particular, at the FM/oxide interface, the 3*d* electronic states are tuned via the hybridization with oxygen states; this suggests the possibility of having transition-metal oxide with high magnetic anisotropy.

In 3*d* transition-metal oxides, the hybridization of metal 3*d* and oxygen 2*p* states generates a crystal-field splitting  $\Delta \sim 1$  eV; the spin-orbit coupling ( $\xi \sim 50$  meV) couples these split states and modifies the energy by  $\approx \langle L_z \rangle \xi^2 / \Delta$ , where  $\langle L_z \rangle$  is the average angular momentum projection along the out-of-plane direction. This energy modification,

which gives rise to magnetic anisotropy energy, could reach  $\sim 1$  meV if  $\langle L_z \rangle \sim 1$ ; this is why CoFe<sub>2</sub>O<sub>4</sub>, an insulator, indeed exhibits large magnetic anisotropy ( $\sim 1$  MJ/m<sup>3</sup>) and strong spin-lattice coupling, which can be employed to realize PMA in strained films [10,12–22]. For oxide conductors, however, room temperature ferromagnetism is already rare, not to mention high magnetic anisotropy. Widely studied FM oxide conductors, such as La<sub>0.7</sub>Sr<sub>0.3</sub>MnO<sub>3</sub>, unfortunately have low magnetic anisotropy and weak spin lattice coupling due to the dominant  $z^2$  state which has a low orbital angular momentum [23].

Inverse spinel NiCo<sub>2</sub>O<sub>4</sub> (NCO) has recently been demonstrated to be conducting due to the mixed valence [24,25], and ferrimagnetic [24,26–28] from the antialignment of Ni and Co moments above room temperature. In this work, we demonstrate that NCO has a remarkable magnetic anisotropy and spin-lattice coupling which can be employed to generate PMA up to 0.23 MJ/m<sup>3</sup> with a −0.3% epitaxial strain (Fig. 1). Analysis of the microscopic origin of the magnetic anisotropy and the spin-lattice coupling based on single-ion anisotropy reveals the key role of the  $x^2$ - $y^2$  states in Co atoms on the tetrahedra sites.

Pulsed laser deposition was employed to grow epitaxial NCO films between 15 and 20 nm on (001), (110), and (111)-oriented nonmagnetic MgAl<sub>2</sub>O<sub>4</sub> (MAO) substrates ( $a = 8.089$  Å for MAO, 8.114 Å for NCO, in-plane strain  $e_{in} = -0.3\%$ ). Film growth was conducted with 20 mTorr O<sub>2</sub> pressure, 360 °C substrate temperature, 5-cm target-to-substrate distance, using a KrF excimer laser (248 nm, 10 Hz, and 2.5 J/cm<sup>2</sup>). Postgrowth annealing was carried out *ex situ* in 1 atmosphere O<sub>2</sub> at 500 °C. The crystallinity, thickness, and lattice constants of the films were measured using x-ray diffraction (XRD) with a Rigaku D/Max-B x-ray diffractometer ( $\lambda = 1.789$  Å) and a Rigaku SmartLab x-ray diffractometer ( $\lambda = 1.54$  Å). The dependences of magnetization on temperature and magnetic field were measured in a Quantum Design MPMS system. In-plane magnetic anisotropy of NCO (111)

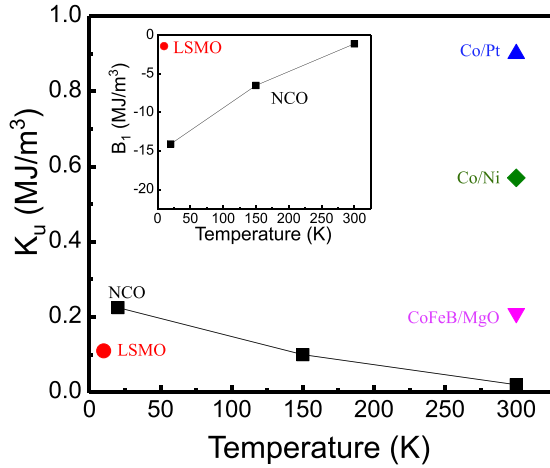


FIG. 1. Uniaxial magnetic anisotropy energy  $K_u$  of strained  $\text{NiCo}_2\text{O}_4$  ( $-0.3\%$ ) and  $\text{La}_{0.7}\text{Sr}_{0.3}\text{MnO}_3$  ( $-2.1\%$ ) films, Co/Pt and Co/Ni multilayers, and CoFeB/MgO heterostructures. Inset: magnetoelastic coupling coefficient  $B_1$  of  $\text{NiCo}_2\text{O}_4$  and  $\text{La}_{0.7}\text{Sr}_{0.3}\text{MnO}_3$ .

films was studied using a home-built magneto-optical Kerr effect (MOKE) system at room temperature in a longitudinal configuration with a rotational sample stage (see Sec. 2, Fig. S2 in Ref. [29] for MOKE details).

XRD shows an epitaxial growth of an NCO (001) film on MAO (001) substrates with no observable impurity phases [Fig. 2(a)]. The Laue oscillations around the (004) peak suggest a high film quality and a thickness of 17 nm for the displayed film. Reciprocal space mapping [Fig. 2(b)] indicate that the film is fully strained since the in-plane lattice constants of the NCO film coincide with that of the MAO substrate. The NCO peak positions in Fig. 2(a), and that in Fig. 2(b), indicate an out-of-plane strain  $e_{\text{out}} = 1.3\%$ . For the (110) and (111) oriented films of similar thickness,  $e_{\text{out}}$  is 0.8% and 0.6%, respectively (see Sec.1, Fig. S1 in Ref. [29] for additional superconducting quantum interference device, XRD data).

Temperature dependence of the magnetization ( $M$ - $T$ ) measured while cooling in a 100 Oe out-of-plane magnetic field shows an upturn [Fig. 2(c)], indicating a transition to magnetic ordering at  $T_C = 323$  K. Figure 2(d) shows a clear square magnetization-field ( $M$ - $H$ ) hysteresis loops at 150 K, with an out-of-plane magnetic field (along the [001] axis); the coercivity is 450 Oe and the remnant magnetization is 94% of the saturation value. In contrast, the  $M$ - $H$  relation has no significant remanence and no measurable coercivity with an in-plane field (along the [100] or [010] axes); the saturation field is 20 kOe. The distinct in-plane and out-of-plane  $M$ - $H$  relations reveal PMA in the NCO (001) films, where [001] is the easy axis. By comparing the  $M$ - $H$  relations with in-plane and out-of-plane magnetic fields, one can extract the anisotropy energy  $K_u$  for the PMA of NCO (001) [Fig. 1].

The PMA in the NCO (001) films, can be understood as a result of spin-lattice coupling and the broken cubic symmetry due to the biaxial epitaxial strain. On a phenomenological level, spin-lattice coupling can be described as magnetoelastic

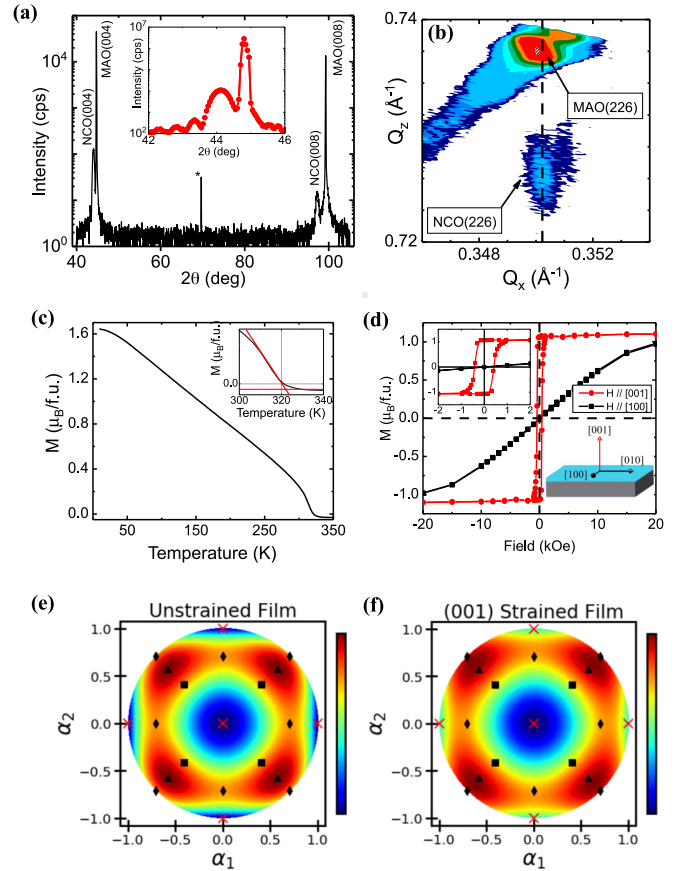


FIG. 2. Structural and magnetic behavior of (001)-oriented films. (a)  $\theta$ - $2\theta$  scan of NCO/MAO (001). Inset is a scan of the NCO (004) peak. (b) Reciprocal space mapping of (226) peaks of NCO and MAO. Alignment of peaks along the  $Q_x$  axis indicates in-plane lattice matching of the film to the MAO substrate. (c)  $M$ - $T$  curve of NCO/MAO(001) film field-cooled in a 100 Oe out-of-plane magnetic field. The inset shows the upturn of magnetization occurring at  $T_C = 323$  K. (d)  $M$ - $H$  relations at 150 K. The upper-left inset shows magnetization behavior closer to the origin. Lower-right inset shows a sketch of the sample. The magnetic anisotropy energy  $F(\alpha_1, \alpha_2)$  of a cubic material without strain (e), and with a compressive biaxial strain in the (001) plane (f), is calculated from the Landau theory. The cross, diamond, square, and triangle symbols indicate the [100], [110], [112], and [111] directions or their cubic equivalent, respectively. The calculation uses the experimentally determined values of constants  $B_1/K_1 = -11.96$  and  $B_2/K_1 = -18.45$ .

effect with the Landau theory using free energy

$$F = K_1(\alpha_1^2\alpha_2^2 + \alpha_2^2\alpha_3^2 + \alpha_3^2\alpha_1^2) + B_1(\alpha_1^2e_{xx} + \alpha_2^2e_{yy} + \alpha_3^2e_{zz}) + B_2(\alpha_1\alpha_2e_{xy} + \alpha_2\alpha_3e_{yz} + \alpha_3\alpha_1e_{zx}), \quad (1)$$

where  $K_1$  is the magnetic anisotropy constant,  $\alpha_1$ ,  $\alpha_2$ , and  $\alpha_3$  are the directional cosines of the magnetization with respect to the  $x$ ,  $y$ , and  $z$  axes, respectively ( $\sum\alpha_i^2 = 1$ ),  $e_{ij}$  are components of the strain tensor,  $B_1$  and  $B_2$  are the longitudinal and shear magnetoelastic coupling constants, respectively. The first term in Eq. (1) corresponds to the magnetic anisotropy of cubic symmetry, while the second and third terms described the magnetoelastic coupling. Without strain ( $e_{ij}=0$ ), if  $K_1 > 0$ ,

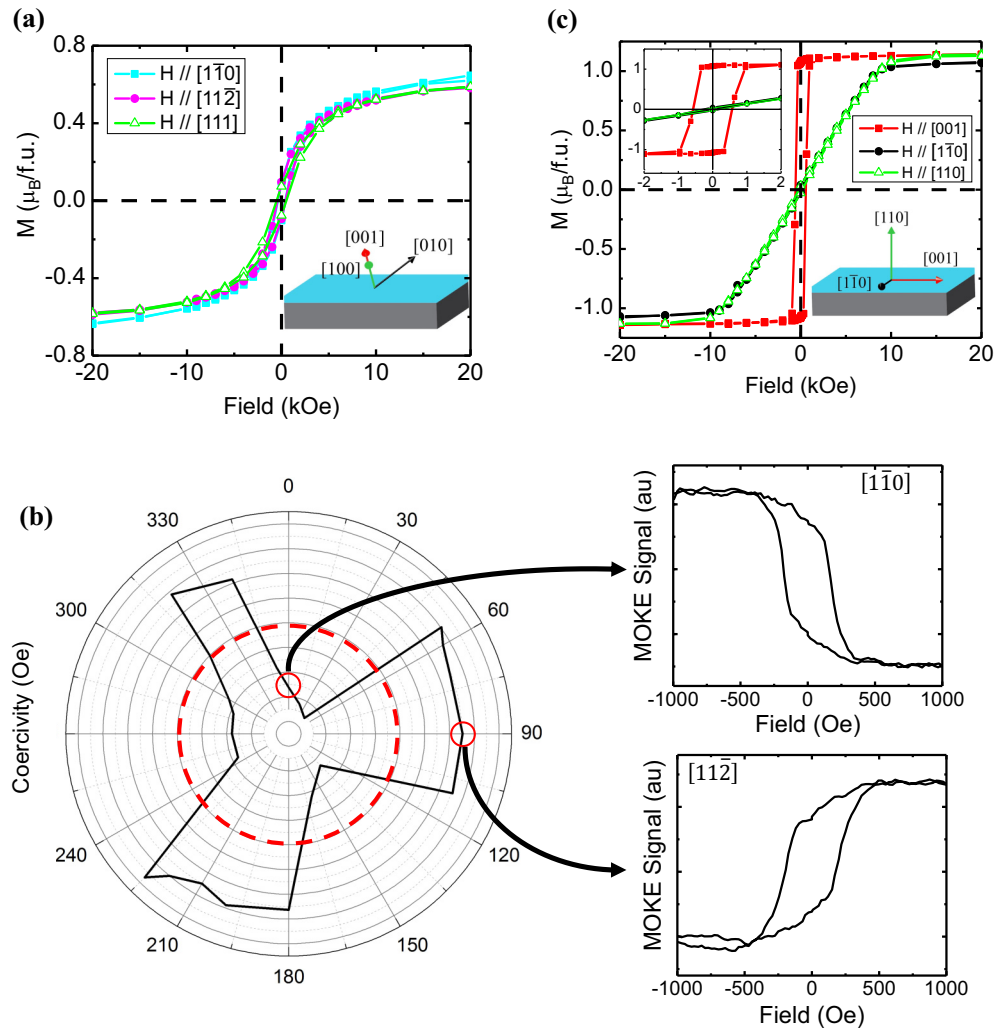


FIG. 3. Magnetic behavior of (111)- and (110)-oriented NCO films. (a)  $M$ - $H$  relation along the out-of-plane and two in-plane directions of the (111)-oriented films measured at 150 K. Inset is a schematic of the (111)-oriented film. (b) Polar plot of the coercivities of the hysteresis loops measured using MOKE at room temperature (see text). The red dashed circle indicates zero coercivity, i.e., values outside the circle have a hysteresis loop with positive saturation at high fields (“normal”), while values inside the circle have a hysteresis loop with positive saturation at negative fields (“inverted”). Examples of each type of loop are shown at the angles. The corresponding crystallographic direction along which the magnetic field is applied is shown on the individual plots. (c)  $M$ - $H$  relation at 150 K for the (110)-oriented films. Upper-left inset further shows magnetization behavior closer to the origin. Lower-right inset shows a sketch of the sample with axes labeled.

by minimizing  $F$ , one finds that the global easy axes are  $[100]$ ,  $[010]$ , and  $[001]$ , which are equivalent under the cubic symmetry (see Fig. S5 in Ref. [29]); the global hard axes are along  $[111]$  axis or its equivalent. These results can be visualized in Fig. 2(e), where the easy (hard) axes correspond to the energy minima (maxima).

For the NCO/MAO (001) films (nonzero strain:  $e_{xx} = e_{yy} = e_{in} < 0$ ,  $e_{zz} = e_{out} > 0$ ), the free energy along the  $[100]$  and  $[001]$  axis are  $F_{[100]} = B_1 e_{xx}$  and  $F_{[001]} = B_1 e_{zz}$ , respectively; the observed easy axis along the  $[001]$  direction [Fig. 2(d)] requires  $F_{[001]} < F_{[100]}$  or  $B_1 < 0$ , as illustrated in Fig. 2(f).

To fully characterize the magnetic anisotropy and the magnetoelastic effect, we also studied the  $M$ - $H$  relations for the (111) and (110)-oriented NCO films.

The  $M$ - $H$  relation of the NCO (111) films with in-plane and out-of-plane field directions, all show an “S” shaped

loop with a small remanence (12%–15%) and coercivity (700 Oe along  $[111]$ ; 500 Oe along other directions) [Fig. 3(a)], indicating that they are not easy axes. The easy axis is most likely tilted with non-zero projections in both in-plane and out-of-plane directions. To investigate the tilted easy axes, we carried out MOKE measurement using the longitudinal mode, which measures the projection of magnetization in the direction of the reflected light. Using this method, one may observe a normal or an inverse  $M$ - $H$  hysteresis loop, when the in-plane azimuthal angle between the easy axis and the reflected light are less than or greater than  $\pi/2$ , respectively (see Sec. 2, Fig. S3 in Ref. [29] for further visualization). As shown in Fig. 3(b), both normal and inverse  $M$ - $H$  loops were observed when the film was rotated about the  $[111]$  axis. Using a negative coercivity to distinguish the inverse  $M$ - $H$  loops from the normal ones, the in-plane anisotropy can be visualized using the polar plot of the coercivity [Fig. 3(b)],

TABLE I. Magnetic anisotropy and magnetoelastic coupling coefficient of NiCo<sub>2</sub>O<sub>4</sub> measured in this work.

$K_u$ (MJ/m <sup>3</sup> )	$K_1$ (MJ/m <sup>3</sup> )	$B_1$ (MJ/m <sup>3</sup> )	$B_2$ (MJ/m <sup>3</sup> )
0.23 (20 K)		-14.1 (20 K)	
0.1 (150 K)	0.54 (150 K)	-6.5 (150 K)	-10 (150 K)
0.02 (300 K)	0.08 (300 K)	-1.1 (300 K)	-1.5 (300 K)

where the larger coercivity means closer to the easy axis. A triangular symmetry is revealed, and the in-plane projection of the easy axis appears to be along the [11 $\bar{2}$ ] (or equivalent) directions. The [100], [010], and [001] directions satisfy the geometric symmetry for the easy axes observed in Fig. 3(b).

For the NCO/MAO (111) films, the nonzero strain is  $e_{xy} = e_{yz} = e_{zx} = -e_{in} > 0$ . According to Eq. (1), a positive (negative)  $B_2$  suggests that the compressive strain increases (decreases) the energy of the [111] axis. Experimentally, the measured hysteresis along the out-of-plane direction [111] and the in-plane directions [11 $\bar{2}$ ] are similar [Fig. 3(a)], suggesting that the energy of the [111] direction is reduced from the global maximum, indicating that  $B_2 < 0$ . The free energies of the [100], [010], and [001] axes are not affected since all the longitudinal strains ( $e_{xx}$ ,  $e_{yy}$ , and  $e_{zz}$ ) are zero. For small strain, the global easy axes remain close to these directions, consistent with the MOKE observation (see Fig. S5(d) in Ref. [29]).

The  $M$ - $H$  relation of the NCO (110) films exhibits a slightly canted shape with a coercivity of 550 Oe and remnant magnetization 91% of saturation magnetization when the magnetic field is along the [100] in-plane direction. In contrast, when the magnetic field is along the in-plane [1-10] and out-of-plane [110] directions, the  $M$ - $H$  relation has a minimal hysteresis with a saturation field 10 kOe. For the NCO/MAO (110) films, the nonzero strain is  $e_{xx} = e_{yy} = (e_{in} + e_{out})/2 > 0$ ,  $e_{zz} = e_{in} < 0$ , and  $e_{xy} = (e_{out} - e_{in})/2 > 0$ . The free energies of the [100] and [010] axes reduce, while that of [001] axis increases, because  $B_1 < 0$ . Therefore, [001] becomes a local easy axis, consistent with slightly canted  $M$ - $H$  loop measured when the field is along the in-plane [001] axis, while the global easy axes remain close to the [100] and [010] directions (see Fig. S5(c) in Ref. [29]).

One may determine  $K_1$ ,  $B_1$ , and  $B_2$  from the magnetic anisotropy energy extracted from the  $M$ - $H$  relations for the NCO films of different orientations. The results are listed in Table I, as well as in Fig. 1. The tunability of the magnetic anisotropy is highlighted by the large magnetoelastic coupling coefficients  $B_1$  and  $B_2$ .

Next, we analyze the microscopic origin of the spin-lattice coupling in terms of the effect of strain on the single-ion magnetic anisotropy energy via the spin-orbit coupling. We employ a model Hamiltonian using a one-electron picture

$$H = \sum_i \left[ \frac{p_i^2}{2m} - \frac{Ze}{4\pi\epsilon_0 r_i} + V_{CF} + \xi \vec{S}_i \cdot \vec{l}_i + E_{ex} \vec{S}_i \cdot \hat{B}_{ex} \right], \quad (2)$$

where  $p_i$ ,  $l_i$ ,  $S_i$ ,  $\vec{r}_i$  are momentum, orbital angular momentum, spin, and position vector of the  $i$ th electron,  $-\frac{Ze}{4\pi\epsilon_0 r_i}$  and

$V_{CF}(\vec{r}_i)$  are the potential energy due to the ion core and the crystal field, respectively,  $\hat{B}_{ex}$  is an exchange field that generates the energy gap  $E_{ex}$  between spins of opposite directions,  $e$ ,  $m$ ,  $\epsilon_0$ ,  $g$ ,  $\hbar$  are the electronic charge, electronic mass, vacuum permittivity, Landé g-factor, and reduced Planck constant. The spin-lattice coupling can be understood as that the strain modifies the electronic orbital states by changing the local environment of the magnetic ions ( $V_{CF}$ ), followed by the change of their preferred spin orientations due to the spin-orbit coupling.

In the unit cell of NCO, eight low-spin Ni<sup>3- $\delta$</sup>  ions and eight high-spin Co<sup>2+ $\delta$</sup>  ions are in NiO<sub>6</sub> octahedra [Fig. 4(a),  $O_h$  symmetry] and CoO<sub>4</sub> tetrahedra [Fig. 4(b),  $T_d$  symmetry], respectively, where  $\delta < 1$ , which indicates the mixed valences [24,25]. The other eight CoO<sub>6</sub> octahedra contain low-spin Co<sup>3+</sup>, which do not contribute to magnetism. The Co and Ni 3d states are split into doubly degenerate  $e_g$  states and triply degenerate  $t_{2g}$  states due to the corresponding  $V_{CF}$ . Under the biaxial compressive strain which reduces the cubic symmetry to tetragonal, these states further split [Figs. 4(a) and 4(b); see Sec. 5 in Ref. [29] for derivation].

We simulate the crystal field by replacing the oxygen atoms with point charges in NiO<sub>6</sub> and CoO<sub>4</sub>. The total energy on a magnetic ion  $E_t$  is calculated by summing the energy of the individual electrons [6] according to the population in Figs. 4(a) and 4(b), where  $\delta = 0.5$  is assumed. The single-ion magnetic anisotropy manifests in the dependence of  $E_t$  on the direction of  $\hat{B}_{ex}$ . As an example, for in the (001) NCO films, the single-ion magnetic anisotropy is defined as  $E_{SIMA} = E_{t,x} - E_{t,z}$ , where  $E_{t,x}$  and  $E_{t,z}$  are  $E_t$  when  $\hat{B}_{ex}$  is along the  $x$  (in-plane) and  $z$  (out-of-plane) axes, respectively. The epitaxial strain  $\Delta a/a$ , where  $a$  is the bulk lattice constant, is introduced by distorting the NiO<sub>6</sub> and CoO<sub>4</sub> local environment according to the lattice constant change, which are  $\Delta a$  and  $-2\Delta a$  for in-plane and out-of-plane axes, respectively. The simulated  $E_{SIMA}$  as a function of strain is shown in Fig. 4(c). For both Ni<sup>3- $\delta$</sup>  and Co<sup>2+ $\delta$</sup> , under the compressive strain ( $\Delta a < 0$ ), which generates a tetragonal distortion,  $E_{SIMA}$  is positive, suggesting that the  $c$  axis (out-of-plane direction) is the easy axis, which is consistent with the experimental observation.

To reveal more microscopic detail of the effect of strain on magnetic anisotropy, here we analyze Co<sup>2+ $\delta$</sup> O<sub>4</sub> tetrahedra as an example since it shows a larger effect in Fig. 4(c). In this case, the 3d electronic configuration can be viewed as a half-filled shell plus an electron in the  $|x^2-y^2\rangle$  state and a fractional occupation in the  $z^2$  state, due to the tetragonal distortion that generates an  $S_4$  symmetry, as shown in Figs. 4(b) and 4(d). Since the half-filled shell is not expected to contribute to the magnetic anisotropy, the electron in the  $|x^2-y^2\rangle$  state dominates the anisotropy. As illustrated in Fig. 4(d), if the spin is along the  $z$  axis, the  $|x^2-y^2, S_z = 1/2\rangle$  state couples to the  $|xy, S_z = 1/2\rangle$  state to lower its energy with a coupling strength  $\langle x^2-y^2, S_z = 1/2 | \xi \vec{S}_i \cdot \vec{l}_i | xy, S_z = 1/2 \rangle = \xi$ . On the other hand, when the spin is along the  $x$  axis, the  $|x^2-y^2, S_x = 1/2\rangle$  state couples to the  $|xz, S_x = 1/2\rangle$  state to lower its energy with a coupling strength  $\langle x^2-y^2, S_x = 1/2 | \xi \vec{S}_i \cdot \vec{l}_i | xz, S_x = 1/2 \rangle = \xi/2$ , which is smaller than that when the spin is along the  $c$  axis. Therefore, the compressive strain results in an out-of-plane magnetic anisotropy. Hence,

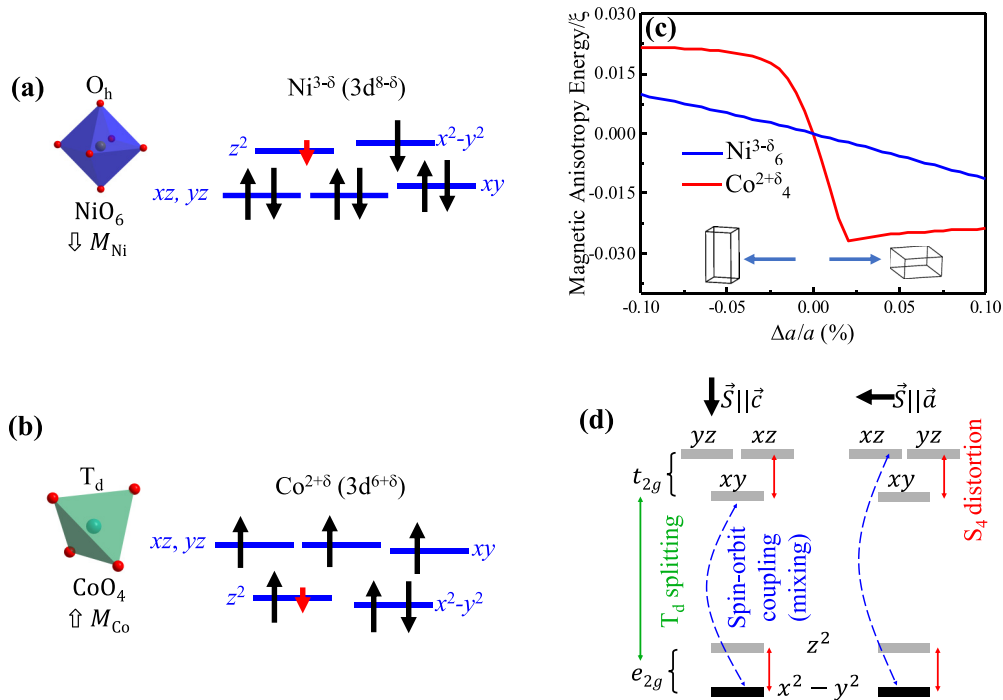


FIG. 4. Microscopic model of the effect of the biaxial strain in the (001) plane. (a), (b) Octahedral and tetrahedral environments of magnetic nickel and cobalt sites, respectively. The energy diagrams show the splitting between the  $e_g$  and  $t_{2g}$  levels, as well as the smaller splitting within the symmetry groups due to the tetragonal strain distortions. The short arrows represent partial ( $\delta$ ) occupation of the orbital. (c) The magnetic anisotropy energy calculated from the single-ion magnetic anisotropy as a function of in-plane biaxial strain, where  $\xi = 50$  meV is the spin-orbit coupling constant; the magnitude of  $V_{\text{CF}}$  and  $E_x$  are set as 1 and 5 eV, respectively. (d) Relative energies of mixing states due to the spin-orbit coupling. The energy gain is larger when the spin is along the  $c$  axis than that when the spin is perpendicular to the  $c$  axis, leading to magnetocrystalline anisotropy.

the  $3d |x^2-y^2\rangle$  state of Co in the  $\text{Co}^{2+\delta}\text{O}_4$ , plays a key role in the spin-lattice coupling of NCO due to its potentially large orbital angular momentum along the  $z$  axis. Assuming the magnitude of  $\xi$ ,  $V_{\text{CF}}$ , and  $E_{\text{ex}}$  as 0.05, 1, and 5 eV respectively, the single-ion magnetic anisotropy is found to be  $\sim 1$  meV per formula unit, as show in Fig. 4(c); this translates to  $\sim 1$  MJ/m<sup>3</sup> in magnetic anisotropy energy, in fair agreement with the observed values in Table I.

In conclusion, we have demonstrated a remarkable PMA in the (001)-oriented NCO/MAO epitaxial films above room temperature which can be understood as a result of the spin-lattice coupling manifested as magnetoelastic effect. The microscopic origin of spin-lattice coupling has been explained using the effect of strain on the single-ion magnetic anisotropy energy due to spin-orbit coupling. The demonstration and elucidation of the strong tunability of magnetic anisotropy in NCO, indicate the possibility of high PMA in oxide conductors. This adds material structures, such as a NCO/MAO/NCO tunnel junction of enhanced magnetoresistance [30] into

nanoscale spintronic devices. In addition, it opens up another route toward electrical and mechanical control of magnetism [31] above room temperature.

## ACKNOWLEDGMENTS

This project was primarily supported by the National Science Foundation (NSF), DMR under Award No. DMR-1454618. C.S. acknowledges the support by the Nebraska Center for Energy Sciences Research on magnetic imaging. J.W. acknowledges the support of REU program of Nebraska Center for Materials and Nanoscience on magneto-optical studies. The research was performed in part in the Nebraska Nanoscale Facility: National Nanotechnology Coordinated Infrastructure, and the Nebraska Center for Materials and Nanoscience, which are supported by the National Science Foundation under Award No. ECCS: 1542182, and the Nebraska Research Initiative.

[1] B. Tudu and A. Tiwari, *Vacuum* **146**, 329 (2017).

[2] R. Sbiaa, H. Meng, and S. N. Piramanayagam, *Phys. Status Solidi - Rapid Res. Lett.* **5**, 413 (2011).

[3] A. Sakuma, *J. Phys. Soc. Japan* **63**, 3053 (1994).

[4] G. H. O. Daalderop, P. J. Kelly, and M. F. H. Schuurmans, *Phys. Rev. B* **44**, 12054 (1991).

[5] A. B. Shick and O. N. Mryasov, *Phys. Rev. B* **67**, 172407 (2003).

- [6] G. H. O. Daalderop, P. J. Kelly, and F. J. A. den Broeder, *Phys. Rev. Lett.* **68**, 682 (1992).
- [7] P. F. Carcia, *J. Appl. Phys.* **63**, 5066 (1988).
- [8] B. Dieny and M. Chshiev, *Rev. Mod. Phys.* **89**, 025008 (2017).
- [9] J. M. D. Coey, *Magnetism and Magnetic Materials* (Cambridge University Press, Cambridge, 2010).
- [10] F. Eskandari, S. B. Porter, M. Venkatesan, P. Kameli, K. Rode, and J. M. D. Coey, *Phys. Rev. Mater.* **1**, 074413 (2017).
- [11] S. Ikeda, K. Miura, H. Yamamoto, K. Mizunuma, H. D. Gan, M. Endo, S. Kanai, J. Hayakawa, F. Matsukura, and H. Ohno, *Nat. Mater.* **9**, 721 (2010).
- [12] D. Fritsch and C. Ederer, *Phys. Rev. B* **82**, 104117 (2010).
- [13] B. H. Liu and J. Ding, *Appl. Phys. Lett.* **88**, 042506 (2006).
- [14] T. Niizeki, Y. Utsumi, R. Aoyama, H. Yanagihara, J. Inoue, Y. Yamasaki, H. Nakao, K. Koike, and E. Kita, *Appl. Phys. Lett.* **103**, 162407 (2013).
- [15] A. Lisfi and C. M. Williams, *J. Appl. Phys.* **93**, 8143 (2003).
- [16] A. Lisfi, C. M. Williams, L. T. Nguyen, J. C. Lodder, A. Coleman, H. Corcoran, A. Johnson, P. Chang, A. Kumar, and W. Morgan, *Phys. Rev. B* **76**, 054405 (2007).
- [17] W. Huang, J. Zhu, H. Z. Zeng, X. H. Wei, Y. Zhang, and Y. R. Li, *Appl. Phys. Lett.* **89**, 262506 (2006).
- [18] X. S. Gao, D. H. Bao, B. Birajdar, T. Habisreuther, R. Mattheis, M. A. Schubert, M. Alexe, and D. Hesse, *J. Phys. D* **42**, 175006 (2009).
- [19] W. H. Wang and X. Ren, *J. Cryst. Growth* **289**, 605 (2006).
- [20] A. V. Ramos, T. S. Santos, G. X. Miao, M.-J. Guittet, J.-B. Moussy, and J. S. Moodera, *Phys. Rev. B* **78**, 180402(R) (2008).
- [21] A. Raghunathan, I. C. Nlebedim, D. C. Jiles, and J. E. Snyder, *J. Appl. Phys.* **107**, 09A516 (2010).
- [22] J. Inoue, T. Niizeki, H. Yanagihara, H. Itoh, and E. Kita, *AIP Adv.* **4**, 027111 (2014).
- [23] Z. Xiao, F. Zhang, M. A. Farrukh, R. Wang, G. Zhou, Z. Quan, and X. Xu, *J. Mater. Sci.* **54**, 9017 (2019).
- [24] Y. Bitla, Y. Chin, J.-C. Lin, C. N. Van, R. Liu, Y. Zhu, H. Liu, Q. Zhan, H. Lin, C. Chen, Y. Chu, and Q. He, *Sci. Rep.* **5**, 15201 (2015).
- [25] C. Zhen, X. Zhang, W. Wei, and W. Guo, *J. Phys. D* **51**, 145308 (2018).
- [26] X. Chen, X. Zhang, M. Han, L. Zhang, Y. Zhu, X. Xu, and X. Hong, *Adv. Mater.* **31**, 1805260 (2018).
- [27] P. Silwal, C. La-o-vorakiat, E. E. M. Chia, D. H. Kim, and D. Talbayev, *AIP Adv.* **3**, 092116 (2013).
- [28] P. Silwal, L. Miao, J. Hu, L. Spinu, D. Ho Kim, and D. Talbayev, *J. Appl. Phys.* **114**, 103704 (2013).
- [29] See Supplemental Material at <http://link.aps.org/supplemental/10.1103/PhysRevB.101.014413> for additional information regarding magnetic and structural data, MOKE measurements, MFM images, phenomenological treatment, and microscopic Hamiltonian derivation.
- [30] H. Sukegawa, Y. Miura, S. Muramoto, S. Mitani, T. Niizeki, T. Ohkubo, K. Abe, M. Shirai, K. Inomata, and K. Hono, *Phys. Rev. B* **86**, 184401 (2012).
- [31] A. Rajapitamahuni, L. Zhang, M. A. Koten, V. R. Singh, J. D. Burton, E. Y. Tsybal, J. E. Shield, and X. Hong, *Phys. Rev. Lett.* **116**, 187201 (2016).